AGU PUBLICATIONS

Geophysical Research Letters

RESEARCH LETTER
10.1002/2016GL069279

Key Points:
- Dynamic oil shale imaging under pyrolysis conditions is performed using synchrotron X-ray microtomography
- 3-D visualization and quantification of the pore space is performed as a function of temperature and time in organic-rich and organic-lean regions
- Microscale disconnected pores are first observed at 390 degrees Celsius; the porosity increases dramatically between 390 and 400 degrees Celsius and becomes connected

Supporting Information:
- Supporting Information S1

Correspondence to:
Q. Lin,
q.lin11@imperial.ac.uk

Citation:
Saif, T., Q. Lin, K. Singh, B. Bijeljic, and M. J. Blunt (2016), Dynamic imaging of oil shale pyrolysis using synchrotron X-ray microtomography, *Geophys. Res. Lett.*, *43*, 6799–6807, doi:10.1002/2016GL069279.

Received 20 APR 2016
Accepted 1 JUN 2016
Accepted article online 3 JUN 2016
Published online 2 JUL 2016

Dynamic imaging of oil shale pyrolysis using synchrotron X-ray microtomography

Tarik Saif[1], Qingyang Lin[1], Kamaljit Singh[1], Branko Bijeljic[1], and Martin J. Blunt[1]

[1]Department of Earth Science and Engineering, Imperial College London, London, UK

Abstract The structure and connectivity of the pore space during the pyrolysis of oil shales determines hydrocarbon flow behavior and ultimate recovery. We image the time evolution of the pore and microfracture networks during oil shale pyrolysis using synchrotron X-ray microtomography. Immature Green River (Mahogany Zone) shale samples were thermally matured under vacuum conditions at temperatures up to 500°C while being periodically imaged with a 2 μm voxel size. The structural transformation of both organic-rich and organic-lean layers within the shale was quantified. The images reveal a dramatic change in porosity accompanying pyrolysis between 390 and 400°C with the formation of micron-scale heterogeneous pores. With a further increase in temperature, the pores steadily expand resulting in connected microfracture networks that predominantly develop along the kerogen-rich laminations.

1. Introduction

The accelerated growth in global energy demand and the depletion of conventional hydrocarbon resources have created a demand for alternative energy sources [*IEA*, 2015]. Oil shale, a fine-grained organic-rich sedimentary rock, represents a large and mostly untapped unconventional hydrocarbon resource with global reserves estimated at 4.8 trillion barrels [*World Energy Council*, 2013]. The largest known deposit is the Eocene Green River Formation in Western Colorado, Eastern Utah, and Southern Wyoming [*Dyni*, 2003; *Johnson et al.,* 2009]. Kerogen, which constitutes most of oil shale's organic matter, is a highly cross-linked, macromolecular material distributed in a heterogeneous inorganic matrix [*Fletcher et al.,* 2014; *Solum et al.,* 2013]. Pyrolysis of oil shale breaks down the complex kerogen network structure to produce shale oil and natural gas [*Hillier et al.,* 2013; *Sun et al.,* 2014]. To improve our understanding of hydrocarbon transport phenomena involved in the pyrolysis of oil shale, a comprehensive characterization of the changes in petrophysical properties is required: in particular, the development of pore structure and connectivity. In this paper, we present a direct visualization of the temporal evolution of the pore space during pyrolysis.

The application of this study is for oil shale retorting which can be categorized into two types [*Lee et al.,* 2007; *Qian et al.,* 2008; *Soone and Doilov*, 2003]: aboveground (ex situ) and underground (in situ). Ex situ processes involve mining near-surface oil shale deposits and retorting under anaerobic conditions at temperatures near 500°C, for times on the order of an hour [*Han et al.,* 2009; *Lee et al.,* 2007]. On the other hand, in situ retorting technologies involve heating oil shale in the geologic formation in the range of 300–350°C from days to months [*Brandt*, 2008; *Liu et al.,* 2009]. Many studies have been conducted on oil shale pyrolysis to better understand the effect of fundamental parameters on shale oil yield and quality to optimize the reaction conditions. This includes pyrolysis temperature [*Chen and Shi*, 2010; *Williams and Ahmad*, 1999; *Yue et al.,* 2014], heating rate [*Değirmenci and Durusoy*, 2005; *Nazzal*, 2002; *Williams et al.*, 1999; *Yue et al.,* 2014], residence time for pyrolysis reaction [*Williams and Chishti*, 2001], composition of pyrolysis atmosphere [*Netzel and Miknis*, 1982; *Razvigorova et al.,* 2008], particle size [*Ahmad and Williams*, 1998; *Jaber et al.,* 1999; *Khalil*, 2013], and mineral matrix [*Espitalie et al.,* 1980; *Karabakan and Yürüm*, 1998]. Vacuum pyrolysis has been shown to enable higher yield and improved quality shale oil in comparison with pyrolysis under atmospheric pressure [*Hoekstra et al.,* 2012; *Pakdel et al.,* 1999; *Roy et al.,* 1985; *Siramard et al.,* 2016]. A reduced pressure facilitates the transport of pyrolysis products by providing quicker escape of primary oil from the reaction zone, thus reducing the secondary cracking reactions [*Pakdel et al.,* 1999; *Siramard et al.,* 2016].

In this experimental study, we apply vacuum pyrolysis conditions to the organic-rich Mahogany zone oil shale of the Green River Formation to capture the dynamic pore structure development at temperatures representative of ex situ oil shale extraction technologies.

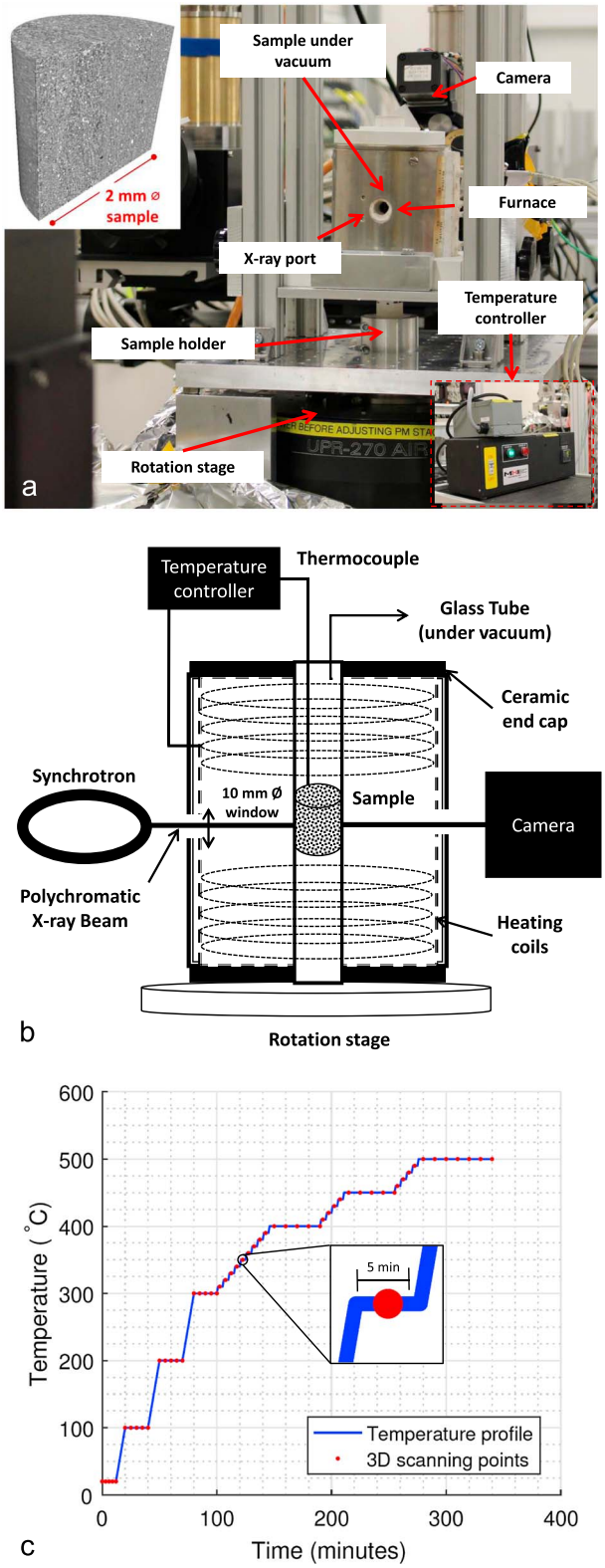

Figure 1. (a) Experimental apparatus used at Diamond Light Source Beamline I13-2 and (b) schematic of experimental apparatus. (c) Temperature profile used in the experiment, with each point (red) representing an acquisition of a 3-D tomogram. In total 52 scans were recorded.

X-ray microcomputed tomography (μCT) has provided direct visualization and quantitative assessment of geological samples [*Andrä et al.,* 2013; *Andrew et al.,* 2013; *Berg et al.,* 2013; *Blunt et al.,* 2013; *Cnudde and Boone*, 2013; *Dann et al.,* 2010; *Ketcham and Carlson*, 2001; *Lin et al.,* 2015, 2016; *Mahabadi et al.,* 2012; *Menke et al.,* 2015; *Singh et al.,* 2016; *Wildenschild and Sheppard*, 2013], including oil shale rocks [*Coshell et al.,* 1994; *Kang et al.,* 2011; *Tiwari et al.,* 2013]. The advantage of μCT is that it allows nondestructive access to the internal structure of objects, providing qualitative and quantitative data about the structure and morphology of 3-D samples and features (pores, fractures, grains, etc.). To capture dynamic processes, recent work has focused on X-ray imaging of geological materials using synchrotron X-ray microtomography [*Andrew et al.,* 2015; *Berg et al.,* 2014; *Fusseis et al.,* 2014; *Madonna et al.,* 2013; *Menke et al.,* 2016; *Panahi et al.,* 2014]. This can be considered as four-dimensional (4-D) tomography (three spatial coordinates plus time evolution), where 3-D tomograms are recorded over a short period of time. Several complex physical and chemical changes occur during the thermal conversion of organic matter in oil shale to produce oil and gas [*Braun and Rothman*, 1975; *Burnham*, 2010; *Kök and Pamir*, 2000; *Na et al.,* 2012]—μCT can complement previous work by quantifying the changes in pore structure and connectivity.

Existing studies on oil shale imaging are limited and have focused primarily on static 3-D imaging. μCT has been applied to oil shale samples from the United States (Green River) [*Tiwari et al.,* 2013], China (Fushun) [*Kang et al.,* 2011], and Australia (Queensland) [*Coshell et al.,* 1994]. *Tiwari et al.* [2013] characterized pore structures before and after pyrolysis based on 42 μm voxel size scans with pores as large as 500 μm observed after pyrolysis. These ex situ studies are limited as they analyze samples before and after an experiment, providing an incomplete understanding of a spatially and temporally dynamic process. To capture this time

dependence, we require fast scanning times, high resolution, at high temperatures and anaerobic conditions. To meet all of these challenges is currently experimentally difficult using laboratory-based μCT systems. Here we present a novel experimental technique using synchrotron imaging to dynamically visualize and quantify the 3-D pore network structure and connectivity for the pyrolysis of oil shale.

2. Materials and Methods

The oil shale sample was obtained from an outcrop of the organic-rich Mahogany zone of the Green River Shale Formation (Uinta Basin, Utah). Thermogravimetric analysis (TGA) has been used extensively as a means of determining pyrolysis characteristics and also to determine kinetic parameters [*Jaber and Probert*, 2000; *Karabakan and Yürüm*, 1998; *Kok*, 2001; *Rajeshwar*, 1981; *Tiwari and Deo*, 2012a, 2012b; *Torrente and Galan*, 2001; *Williams and Ahmad*, 2000]. In this study, TGA of the oil shale sample was conducted using a Perkin-Elmer Pyris 1 instrument (Perkin Elmer, USA) to establish the mass loss profile allowing for comparison with segmented pore volumes from image analysis. A 100 g sample of the oil shale rock was crushed and milled, and 20 mg of this powdered sample was heated to 850°C at a heating rate of 10°C/min using nitrogen as the purge gas.

A 2.5 mm diameter by 10 mm length core was selected from the same oil shale rock which contained organic rich and lean laminations tightly bound in an inorganic mineral-rich matrix. A custom built furnace was used to heat the sample during the experiment. The cylindrical furnace consisted of two viewports on opposite sides to allow the X-ray beam to directly pass through. The sample was loaded into a borosilicate glass tube and placed under vacuum pressure at 0.1 kPa absolute. A thermocouple measured sample temperature and a proportional integral differential (PID) controller regulated the temperature to ±1°C. A detailed schematic of the experimental apparatus is shown in Figure 1.

The experiment was performed at the Diamond Light Source I13-2 beamline with a polychromatic beam energy that ranges from 8 to 30 KeV with a maximum photon flux of 4×10^9 Ph/s. The low-energy X-rays were filtered by passing the beam through 2 mm Al and 0.1 mm Au filters. A 250 μm thick $CdWO_4$ scintillator with a 4X objective lens and a PCO EDGE 5.5 camera were used.

The 3-D scans had an exposure time of 80 ms, capturing 2001 projections as the sample was rotated 180° around an axis perpendicular to the quasi-parallel incident polychromatic X-ray beam. The total acquisition time was 160 s per scan. Figure 1c illustrates the experimental heating profile with each point indicating a tomography scan at the centre of the core with a 2 mm × 2 mm field of view. The sample was heated from 20°C to 500°C with the temperature held constant at key pyrolysis stages where scans were recorded.

Each reconstructed image had 1000^3 voxels with a voxel size of 2 μm. A nonlocal means edge preserving filter [*Buades et al.*, 2005, 2008] was applied to reduce noise (Figures 2a–2d). The pore space was segmented (Figures 2e and 2f) using Otsu's algorithm [*Otsu*, 1979] which maximizes the between-class variance of voxel intensity. For this data set, the algorithm provided consistent segmentation to separate the pore space from the rest of the solid phase. All image processing was conducted using the Avizo 9.0 program (FEI, Visualization Sciences Group) and MATLAB (MathWorks).

3. Results

Figures 2a–2d show 2-D cross-sectional slices of 3-D images of the Green River (Mahogany Zone) oil shale sample, with the gray scale values for each pixel corresponding to X-ray attenuation, which varies as a function of density and atomic number. In Figure 2a, the less dense organic-rich material is shown as the darker colored regions, while the denser mineral-rich matrix appears lighter.

Figure 3 shows the porosity as a function of experimental time given the experimental temperature profile (Figure 1c). Between 20°C and 380°C no visible change in porosity was detected for a 2 μm voxel size. The cross sections (Figures 2b and 2e) reveal the onset of resolvable pores at 390°C in the organic-rich layers of the shale sample with a total sample porosity of 2.7% (Figure 3). To illustrate this, Figure 4 presents 3-D visualizations of the segmented pore structure (Figures 2e and 2f) at 390°C and 400°C. A dramatic increase in total porosity to 21.9% is observed at 400°C as the pores expand resulting in microfracture networks parallel to the shale bedding which provide a pathway for the outgoing hydrocarbons. In Figure 4c we plot the computed porosity values for each vertical slice (A to B) at 390°C and 400°C, revealing a well-defined variation in

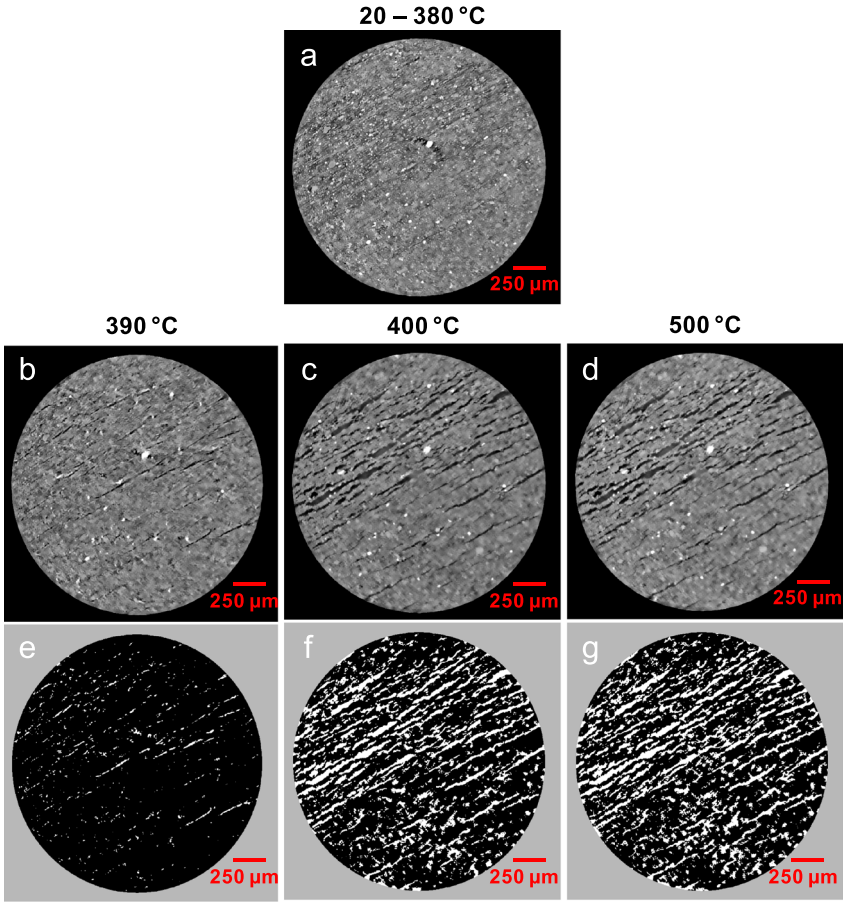

Figure 2. (a–d) Filtered gray scale images at different temperatures. (e–g) Segmented images with pore space shown white. The gray scale cross sections show organic-rich laminations (dark grey) tightly bound in an inorganic mineral matrix (light grey) with no resolvable pore space between 20°C and 380°C. The first resolvable pore space appears at 390°C. There then follows a dramatic increase in porosity to form microfracture networks along the organic-rich laminations (Figures 2c and 2f) with a small but detectable increase in porosity with a further increase in sample temperature to 500°C (Figures 2d and 2e).

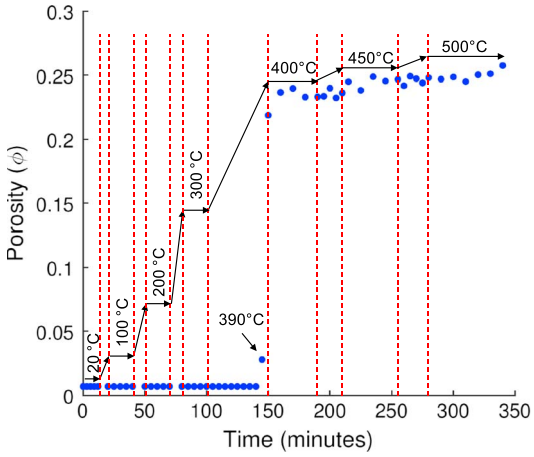

Figure 3. Porosity as a function of experimental time. The temperature is indicated by the arrows. Between 20°C and 380°C no resolvable porosity was observed; at 390°C the first microscale pores were detected contributing to a porosity of 2.7%; at 400°C a dramatic increase in porosity is observed resulting in a total porosity of 21.9%; and a further increase in pyrolysis temperature to 500°C leads to a smaller increase in porosity to 24.9%.

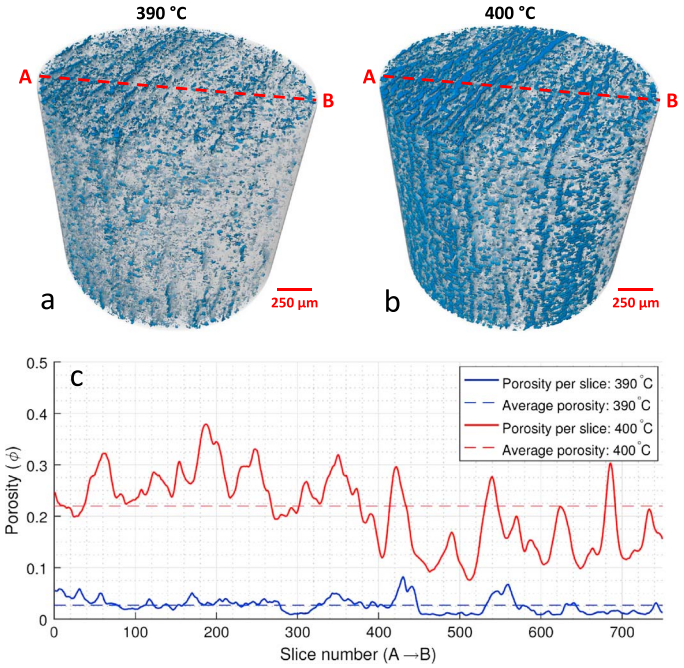

Figure 4. The 3-D rendered volumes of the oil shale sample at (a) 390°C and (b) 400°C. The dramatic increase in porosity is visualized with the pore phase (blue) and remaining matrix phase (gray). The porosity profile across the sample from A to B for both 390°C and 400°C reveals a variable porosity distribution related to the thermal decomposition of organic material.

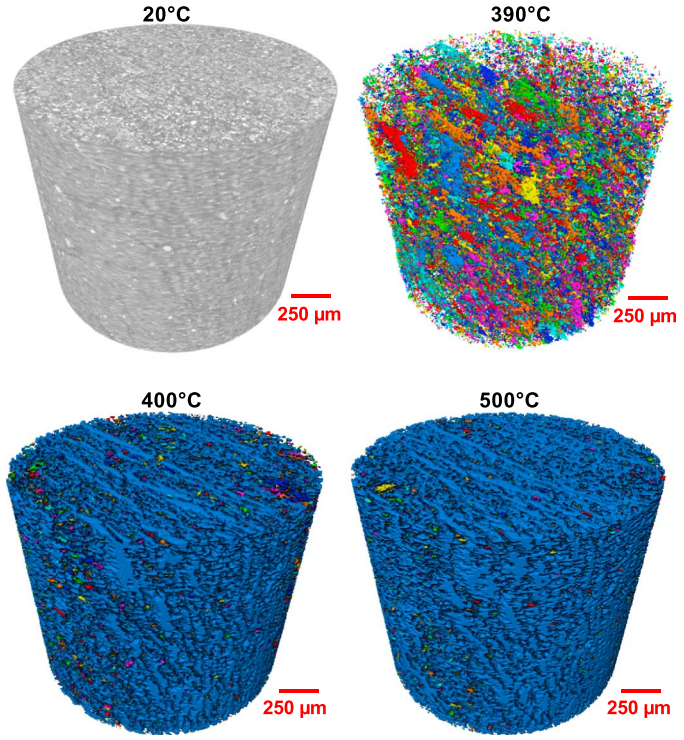

Figure 5. The 3-D rendering of the pore space where the colors indicate clusters of connected pores. At 20°C no pores can be resolved. At 390°C all the pore space appears disconnected at the resolution of the image—the large range of colors indicates a poorly connected pore network. At 400°C and 500°C the vast majority of the pore space is connected, 96.5% and 97.8% respectively, shown in blue.

the spatial porosity distribution after pyrolysis. We observe greater porosity in the organic-rich regions (which we assume are the darker areas at the beginning of the experiment) compared to the organic-lean regions. We performed scanning electron microscopy energy dispersive X-ray spectroscopy (SEM-EDS) analysis to confirm that the darker regions in the gray scale images are indeed organic rich (41% carbon content) relative to matrix material (see supporting information for further details). The increased porosities in the organic-rich regions fundamentally constitute the combined volumes represented primarily by the loss of organic material. With increasing temperature, devolatilization of kerogen increases the internal vapor pressure of large unconnected pores to such an extent that the mechanical strength of the surrounding material can no longer retain the gas, leading to the dramatic porosity changes observed between 390°C and 400°C. A further increase in temperature to 500°C results in only a 3% increase in average porosity to 24.9%.

The first scan at 400°C revealed a total porosity of 21.9% (Figure 3). The sample was held at 400°C with the acquisition of a further four scans every 10 min to examine the impact of time at a constant temperature. We observe a small but noticeable increase of 2.2% in average porosity to 24.1% over a period of 40 min. This indicates the majority of the pore space transformation occurs within the first 10 min of the temperature stabilizing at 400°C.

Figure 5 shows a 3-D rendering of the connectivity of the pore space: at 390°C all the pore space appears disconnected at the resolution of the scan, as indicated by the wide range of colors. However, at 400°C, 96.5% of the pore space is connected, and a further increase in temperature to 500°C results in a 97.8% connected pore space. Figure 6a shows the mass loss for the bulk sample from TGA analysis and the fractional mass loss change between two points which indirectly represents the pyrolysis reaction rate. At temperatures less than 200°C, a small mass loss is observed, primarily due to the evaporation of water, including adsorbed and interlayer water from clay minerals. At a temperature between 250°C and 500°C a major mass loss of 35.4% is observed. Although we obtain a mass loss of 22.6% from the TGA experiment at 380°C, we did not observe pore space development in our images at 2 μm voxel size until a slightly higher temperature is reached (Figure 2a). This can be attributed to pore structure transformation at submicron resolution. The first mass loss stage in Figure 6a represents the decomposition of organic material where chemical bonds linking the organic compounds to the rock matrix are broken and the kerogen macromolecular structure is pyrolyzed yielding simpler and lighter molecules. A single major trough for organic decomposition suggests that one distinguishable process occurs in this temperature range governed by a single global reaction mechanism. At temperatures above 600°C, a further mass loss of 15.2% is observed related to the decomposition of carbonate and clay minerals. In total we observe a mass loss of 50.6%.

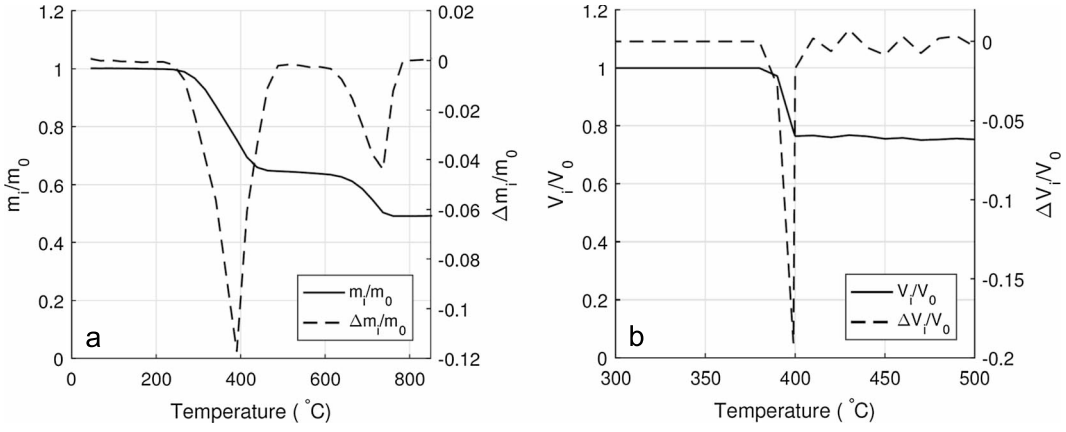

Figure 6. (a) Thermogravimetric (TGA) data showing the fraction of the mass remaining as a function of temperature (solid line) and the fractional change in mass (dashed line) between two measured temperature points. $\boldsymbol{m_0}$ is the initial mass, $\boldsymbol{m_i}$ is the mass at some temperature, and $\Delta\boldsymbol{m_i}$ is the change in mass for a 10°C temperature increase. (b) Image derived data showing the matrix (nonpore) volume loss due to pore space development (solid line) and the fractional change in matrix volume. $\Delta\boldsymbol{V_i}$ is the change in volume for a 10°C temperature increase.

We can relate the fractional mass loss in the TGA analysis to the change in pore volume from the images. Assuming that organic material of a constant density is produced, we may assume that the mass loss is proportional to the increase in pore volume. The fractional change in pore volume as determined from the 3-D images is compared to the change in mass in Figure 6. We obtain a maximum change in oil shale matrix volume at 400°C which is comparable to the maximum change in mass loss for the bulk oil shale sample as measured by TGA. At the 2 μm voxel resolution we have captured the middle-to-late stage of pore space development related to the thermal breakdown of organic matter. To characterize the pore structure evolution at earlier stages of mass loss, images with nanoscale resolution are needed.

4. Conclusions

A novel technique combining synchrotron X-ray tomography with a custom built furnace was designed and applied to visualize and quantify dynamic pore space development for Green River Oil Shale of the organic-rich Mahogany zone at temperatures representative of oil shale pyrolysis technologies (300–500°C). The development in oil shale pore structure during pyrolysis was not resolvable at a voxel size of 2 μm for temperatures between 20°C and 380°C. The onset of resolvable pore space occurred at 390°C in the organic-rich phases with a dramatic increase in porosity and connectivity at 400°C. This striking change in porosity was corroborated by mass loss change determined by TGA. Increasing the temperature further to 500°C resulted in only a small increase in porosity. On holding the temperature constant we observed that the majority of the pore space development took place within the first 10 min. We show that pore development is directly related to the initial spatial distribution of organic matter. Our results provide a direct observation of pore and microfracture development for oil shale pyrolysis to better understand the mechanisms that govern the process to ultimately enhance pyrolysis performance.

Acknowledgments

This work was financially supported by the Imperial College Consortium on Pore-Scale Modelling. We thank Diamond Light Source for beamtime (MT11587) and Principal Beamline Scientist Christoph Rau for his support. The authors are also grateful to Norman Nicholls, Hannah Menke, and Yousef Al-Khulaifi for their experimental support. The images acquired in this study can be downloaded from 10.6084/m9.figshare.3406483.v1

References

Ahmad, N., and P. T. Williams (1998), Influence of particle grain size on the yield and composition of products from the pyrolysis of oil shales, *J. Anal. Appl. Pyrolysis*, *46*(1), 31–49.

Andrä, H., et al. (2013), Digital rock physics benchmarks—Part I: Imaging and segmentation, *Comput. Geosci.*, *50*, 25–32, doi:10.1016/j.cageo.2012.09.005.

Andrew, M., B. Bijeljic, and M. Blunt (2013), Pore-scale imaging of geological carbon dioxide storage under in situ conditions, *Geophys. Res. Lett.*, *40*, 3915–3918, doi:10.1002/grl.50771.

Andrew, M., H. Menke, M. Blunt, and B. Bijeljic (2015), The imaging of dynamic multiphase fluid flow using synchrotron-based X-ray microtomography at reservoir conditions, *Transp. Porous Media*, *110*, 1–24, doi:10.1007/s11242-015-0553-2.

Berg, S., et al. (2013), Real-time 3D imaging of Haines jumps in porous media flow, *Proc. Natl. Acad. Sci. U.S.A.*, *110*(10), 3755–3759.

Berg, S., R. Armstrong, H. Ott, A. Georgiadis, S. Klapp, A. Schwing, R. Neiteler, N. Brussee, A. Makurat, and L. Leu (2014), Multiphase flow in porous rock imaged under dynamic flow conditions with fast X-ray computed microtomography, *Petrophysics*, *55*(04), 304–312.

Blunt, M., B. Bijeljic, H. Dong, O. Gharbi, S. Iglauer, P. Mostaghimi, A. Paluszny, and C. Pentland (2013), Pore-scale imaging and modelling, *Adv. Water Resour.*, *51*, 197–216, doi:10.1016/j.advwatres.2012.03.003.

Brandt, A. R. (2008), Converting oil shale to liquid fuels: Energy inputs and greenhouse gas emissions of the shell in situ conversion process, *Environ. Sci. Technol.*, *42*(19), 7489–7495, doi:10.1021/es800531f.

Braun, R. L., and A. J. Rothman (1975), Oil-shale pyrolysis: Kinetics and mechanism of oil production, *Fuel*, *54*(2), 129–131.

Buades, A., B. Coll, and J. M. Morel (2005), A non-local algorithm for image denoising, in *2005 IEEE Computer Society Conference on Computer Vision and Pattern Recognition (CVPR'05)*, vol. 62, edited by C. Schmid, S. Soatto, and C. Tomasi, pp. 60–65, IEEE, Los Alamos, Calif.

Buades, A., B. Coll, and J.-M. Morel (2008), Nonlocal image and movie denoising, *Int. J. Comput. Vision*, *76*(2), 123–139, doi:10.1007/s11263-007-0052-1.

Burnham, A. K. (2010), Chemistry and kinetics of oil shale retorting, in *Oil Shale: A Solution to the Liquid Fuel Dilemma*, pp. 115–134, Oxford Univ. Press, Oxford.

Chen, M., and Y. Shi (2010), Flash pyrolysis of Fushun oil shale fine particles in an experimental fluidized-bed reactor, *Oil Shale*, *27*(4), 297–308.

Cnudde, V., and M. N. Boone (2013), High-resolution X-ray computed tomography in geosciences: A review of the current technology and applications, *Earth Sci. Rev.*, *123*, 1–17, doi:10.1016/j.earscirev.2013.04.003.

Coshell, L., R. G. McIver, and R. Chang (1994), X-ray computed tomography of Australian oil shales: Non-destructive visualization and density determination, *Fuel*, *73*(8), 1317–1321.

Dann, R., M. Turner, M. Close, and M. Knackstedt (2010), Multi-scale characterisation of coastal sand aquifer media for contaminant transport using X-ray computed tomography, *Environ. Earth Sci.*, *63*(5), 1125–1137, doi:10.1007/s12665-010-0788-8.

Değirmenci, L., and T. Durusoy (2005), Effect of heating rate and particle size on the pyrolysis of Göynük oil shale, *Energy Sources*, *27*(9), 787–795.

Dyni, J. R. (2003), Geology and resources of some world oil-shale deposits, *Rep. 2005-5294*.

Espitalie, J., M. Madec, and B. Tissot (1980), Role of mineral matrix in kerogen pyrolysis: Influence on petroleum generation and migration, *AAPG Bull.*, *64*(1), 59–66.

Fletcher, T. H., R. Gillis, J. Adams, T. Hall, C. L. Mayne, M. S. Solum, and R. J. Pugmire (2014), Characterization of macromolecular structure elements from a Green River oil shale, II. Characterization of pyrolysis products by ^{13}C NMR, GC/MS, and FTIR, *Energy Fuels*, *28*(5), 2959–2970.

Fusseis, F., X. Xiao, C. Schrank, and F. De Carlo (2014), A brief guide to synchrotron radiation-based microtomography in (structural) geology and rock mechanics, *J. Struct. Geol.*, *65*, 1–16, doi:10.1016/j.jsg.2014.02.005.
Han, X., X. Jiang, and Z. Cui (2009), Studies of the effect of retorting factors on the yield of shale oil for a new comprehensive utilization technology of oil shale, *Appl. Energy*, *86*(11), 2381–2385, doi:10.1016/j.apenergy.2009.03.014.
Hillier, J. L., T. H. Fletcher, M. S. Solum, and R. J. Pugmire (2013), Characterization of macromolecular structure of pyrolysis products from a Colorado Green River oil shale, *Ind. Eng. Chem. Res.*, *52*(44), 15,522–15,532.
Hoekstra, E., W. P. M. van Swaaij, S. R. A. Kersten, and K. J. A. Hogendoorn (2012), Fast pyrolysis in a novel wire-mesh reactor: Design and initial results, *Chem. Eng. J.*, *191*, 45–58.
IEA (2015), World Energy Outlook 2015, Rep. [Available at https://www.iea.org/Textbase/npsum/WEO2015SUM.pdf.]
Jaber, J. O., and S. Probert (2000), Non-isothermal thermogravimetry and decomposition kinetics of two Jordanian oil shales under different processing conditions, *Fuel Process. Technol.*, *63*(1), 57–70.
Jaber, J. O., S. D. Probert, and P. T. Williams (1999), Evaluation of oil yield from Jordanian oil shales, *Energy*, *24*(9), 761–781.
Johnson, R. C., T. J. Mercier, M. E. Brownfield, M. P. Pantea, and J. G. Self (2009), Assessment of In-Place Oil shale resources of the Green River Formation, Piceance Basin, Western Colorado, *Rep. 2009-3012*. [Available at http://pubs.er.usgs.gov/publication/fs20093012.]
Kang, Z., D. Yang, Y. Zhao, and Y. Hu (2011), Thermal cracking and corresponding permeability of Fushun oil shale, *Oil Shale*, *28*(2), 273–283.
Karabakan, A., and Y. Yürüm (1998), Effect of the mineral matrix in the reactions of oil shales: 1. Pyrolysis reactions of Turkish Göynük and US Green River oil shales, *Fuel*, *77*(12), 1303–1309.
Ketcham, R. A., and W. D. Carlson (2001), Acquisition, optimization and interpretation of X-ray computed tomographic imagery: Applications to the geosciences, *Comput. Geosci.*, *27*, 381–400, doi:10.1016/S0098-3004(00)00116-3.
Khalil, A. M. (2013), Oil shale pyrolysis and effect of particle size on the composition of shale oil, *Oil Shale*, *30*(2), 136–146.
Kok, M. V. (2001), Thermal investigation of Seyitomer oil shale, *Thermochim. Acta*, *369*(1), 149–155.
Kök, M. V., and M. R. Pamir (2000), Comparative pyrolysis and combustion kinetics of oil shales, *J. Anal. Appl. Pyrolysis*, *55*(2), 185–194.
Lee, S., J. G. Speight, and S. K. Loyalka (2007), *Handbook of Alternative Fuel Technologies*, CRC Press, Boca Raton, Fla.
Lin, Q., S. J. Neethling, K. J. Dobson, L. Courtois, and P. D. Lee (2015), Quantifying and minimising systematic and random errors in X-ray micro-tomography based volume measurements, *Comput. Geosci.*, *77*, 1–7, doi:10.1016/j.cageo.2014.12.008.
Lin, Q., D. J. Barker, K. J. Dobson, P. D. Lee, and S. J. Neethling (2016), Modelling particle scale leach kinetics based on X-ray computed micro-tomography images, *Hydrometallurgy*, *162*, 25–36, doi:10.1016/j.hydromet.2016.02.008.
Liu, D. X., H. Y. Wang, D. W. Zheng, C. H. Fang, and Z. X. Ge (2009), World progress of oil shale in-situ exploitation methods, *Nat. Gas Ind.*, *29*(5), 128–132.
Madonna, C., B. Quintal, M. Frehner, B. S. Almqvist, N. Tisato, M. Pistone, F. Marone, and E. H. Saenger (2013), Synchrotron-based X-ray tomographic microscopy for rock physics investigations, *Geophysics*, *78*(1), D53–D64.
Mahabadi, O. K., N. X. Randall, Z. Zong, and G. Grasselli (2012), A novel approach for micro-scale characterization and modeling of geomaterials incorporating actual material heterogeneity, *Geophys. Res. Lett.*, *39*, L01303, doi:10.1029/2011GL050411.
Menke, H., B. Bijeljic, M. Andrew, and M. Blunt (2015), Dynamic three-dimensional pore-scale imaging of reaction in a carbonate at reservoir conditions, *Environ. Sci. Technol.*, *49*(7), 4407–4414, doi:10.1021/es505789f.
Menke, H., M. Andrew, M. Blunt, and B. Bijeljic (2016), Reservoir condition imaging of reactive transport in heterogeneous carbonates using fast synchrotron tomography—Effect of initial pore structure and flow conditions, *Chem. Geol.*, *428*, 15–26.
Na, J. G., C. H. Im, S. H. Chung, and K. B. Lee (2012), Effect of oil shale retorting temperature on shale oil yield and properties, *Fuel*, *95*, 131–135.
Nazzal, J. M. (2002), Influence of heating rate on the pyrolysis of Jordan oil shale, *J. Anal. Appl. Pyrolysis*, *62*(2), 225–238.
Netzel, D. A., and F. P. Miknis (1982), NMR study of US eastern and western shale oils produced by pyrolysis and hydropyrolysis, *Fuel*, *61*(11), 1101–1109.
Otsu, N. (1979), A threshold selection method from gray-level histograms, *IEEE Trans. Syst. Man Cybern.*, *9*(1), 62–66, doi:10.1109/TSMC.1979.4310076.
Pakdel, H., C. Roy, and W. Kalkreuth (1999), Oil production by vacuum pyrolysis of Canadian oil shales and fate of the biological markers, *Fuel*, *78*(3), 365–375.
Panahi, H., P. Meakin, F. Renard, M. Kobchenko, J. Scheibert, A. Mazzini, B. Jamtveit, A. Malthe-Sorenssen, and D. K. Dysthe (2014), A 4D synchrotron X-ray-tomography study of the formation of hydrocarbon- migration pathways in heated organic-rich shale, *SPE J.*, doi:10.2118/162939-PA.
Qian, J., J. Wang, and S. Li (2008), *World's Oil Shale Available Retorting Technologies and the Forecast of Shale Oil Production*, Int. Soc. of Offshore and Polar Eng., Vancouver, Canada.
Rajeshwar, K. (1981), The kinetics of the thermal decomposition of green river oil shale kerogen by non-isothermal thermogravimetry, *Thermochim. Acta*, *45*(3), 253–263.
Razvigorova, M., T. Budinova, B. Petrova, B. Tsyntsarski, E. Ekinci, and M. F. Ferhat (2008), Steam pyrolysis of Bulgarian oil shale kerogen, *Oil Shale*, *25*(1), 27–37.
Roy, C., B. de Caumia, D. Brouillard, and H. Ménard (1985), The pyrolysis under vacuum of aspen poplar, in *Fundamentals of Thermochemical Biomass Conversion*, edited by R. P. Overend, T. A. Milne, and L. K. Mudge, pp. 237–256, Springer, New York City.
Singh, K., B. Bijeljic, and M. J. Blunt (2016), Imaging of oil layers, curvature and contact angle in a mixed-wet and a water-wet carbonate rock, *Water Resour. Res.*, *52*, 1716–1728, doi:10.1002/2015WR018072.
Siramard, S., L. Lin, C. Zhang, D. Lai, S. Cheng, and G. Xu (2016), Oil shale pyrolysis in indirectly heated fixed bed with internals under reduced pressure, *Fuel Process. Technol.*, *148*, 248–255.
Solum, M. S., C. L. Mayne, A. M. Orendt, R. J. Pugmire, J. Adams, and T. H. Fletcher (2013), Characterization of macromolecular structure elements from a Green River oil shale, I. Extracts, *Energy Fuels*, *28*(1), 453–465.
Soone, J., and S. Doilov (2003), Sustainable utilization of oil shale resources and comparison of contemporary technologies used for oil shale processing, *Oil Shale*, *20*(3), 311–323.
Sun, Y., F. Bai, B. Liu, Y. Liu, M. Guo, W. Guo, Q. Wang, X. Lü, F. Yang, and Y. Yang (2014), Characterization of the oil shale products derived via topochemical reaction method, *Fuel*, *115*, 338–346.
Tiwari, P., and M. Deo (2012a), Detailed kinetic analysis of oil shale pyrolysis TGA data, *AIChE J.*, *58*(2), 505–515.
Tiwari, P., and M. Deo (2012b), Compositional and kinetic analysis of oil shale pyrolysis using TGA–MS, *Fuel*, *94*, 333–341.
Tiwari, P., M. Deo, C. Lin, and J. D. Miller (2013), Characterization of oil shale pore structure before and after pyrolysis by using X-ray micro CT, *Fuel*, *107*, 547–554.
Torrente, M., and M. Galan (2001), Kinetics of the thermal decomposition of oil shale from Puertollano (Spain), *Fuel*, *80*(3), 327–334.

Wildenschild, D., and A. P. Sheppard (2013), X-ray imaging and analysis techniques for quantifying pore-scale structure and processes in subsurface porous medium systems, *Adv. Water Resour.*, *51*, 217–246.
Williams, P. T., and N. Ahmad (1999), Influence of process conditions on the pyrolysis of Pakistani oil shales, *Fuel*, *78*(6), 653–662.
Williams, P. T., and N. Ahmad (2000), Investigation of oil-shale pyrolysis processing conditions using thermogravimetric analysis, *Appl. Energy*, *66*(2), 113–133.
Williams, P. T., and H. M. Chishti (2001), Influence of residence time and catalyst regeneration on the pyrolysis–zeolite catalysis of oil shale, *J. Anal. Appl. Pyrolysis*, *60*(2), 187–203.
World Energy Council (2013), World Energy Resources Survey, Rep. [Available at http://www.worldenergy.org/wp-content/uploads/2013/09/Complete_WER_2013_Survey.pdf.]
Yue, C., Y. Liu, Y. Ma, S. Li, J. He, and D. Qiu (2014), Influence of retorting conditions on the pyrolysis of Yaojie oil shale, *Oil Shale*, *31*(1), 66–78.